

Article

## Reaction Electronic Flux: A New Concept To Get Insights into Reaction Mechanisms. Study of Model Symmetric Nucleophilic Substitutions

Eleonora Echegaray, and Alejandro Toro-Labbe#

*J. Phys. Chem. A*, **2008**, 112 (46), 11801-11807 • DOI: 10.1021/jp805225e • Publication Date (Web): 23 October 2008

Downloaded from <http://pubs.acs.org> on December 5, 2008

### More About This Article

Additional resources and features associated with this article are available within the HTML version:

- Supporting Information
- Access to high resolution figures
- Links to articles and content related to this article
- Copyright permission to reproduce figures and/or text from this article

[View the Full Text HTML](#)



**ACS Publications**  
High quality. High impact.

The Journal of Physical Chemistry A is published by the American Chemical Society, 1155 Sixteenth Street N.W., Washington, DC 20036

# Reaction Electronic Flux: A New Concept To Get Insights into Reaction Mechanisms. Study of Model Symmetric Nucleophilic Substitutions

Eleonora Echegaray and Alejandro Toro-Labbé\*

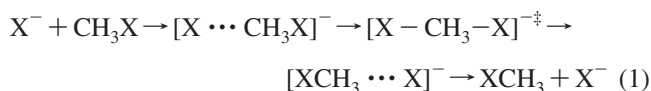
Laboratorio de Química Teórica Computacional (QTC), Facultad de Química, Pontificia Universidad Católica de Chile, Casilla 306, Correo 22, Santiago, Chile

Received: June 13, 2008; Revised Manuscript Received: September 5, 2008

The present work is focused on studying chlorine and fluorine identity  $S_N2$  substitutions on a methyl center, within the framework of the newly introduced reaction electronic flux  $J(\xi)$ , that allows one to identify charge transfer and polarization mechanisms that take place along the reaction coordinate. The main results concern the discovery of different charge transfer mechanism, despite both reactions have the same energetic pattern with simultaneous bond breaking and formation. It turns out that the chlorine substitution is mainly driven by polarization effects and characterized by through bond interactions while intermolecular charge transfer dominates the fluorine exchange reaction, that is characterized by through space interactions.

## 1. Introduction

Bimolecular nucleophilic substitutions ( $S_N2$ ) at carbon centers are one of the most widely studied reactions in organic chemistry.<sup>1</sup> An enormous amount of both experimental<sup>2–5</sup> and theoretical<sup>6–16</sup> work was focused on extracting the intrinsic reactivity properties of many simple organic systems. Studies of halogen exchange in a methyl center (1), became paradigms for the ion–molecule reactivity study.<sup>11,13,16</sup> The one step mechanism presents simultaneous bond breaking and formation at the carbon center, with the classical double well potential and central inversion barrier, due to the formation of stable intermediates: ion-dipole complexes.



Nowadays, energetic and structural parameters of many  $S_N2$  reactions at carbon centers are fully characterized at high theoretical level, for both *ab initio*<sup>14</sup> and density functional theory<sup>12,13</sup>(DFT). In this context, we present a DFT study of the  $CH_3X + X^-$  ( $X = Cl$  and  $F$ ) reactions, aimed at recovering electronic structure information in gas phase, in order to analyze important features of the nucleophilic substitution process along the reaction pathway.

Conceptual DFT<sup>17,18</sup> provides reactivity descriptors of special interest for the study of charge transfer processes, as the chemical potential  $\mu$ ,<sup>19–21</sup> which measures the escaping tendency of an electron cloud from an equilibrium system, in consistency with macroscopic thermodynamics. The derivative of  $\mu$  along the reaction coordinate is the newly introduced reaction electronic flux  $J(\xi)$ ,<sup>22</sup> that characterizes electron density rearrangements between the participating precursors in terms of polarization and net charge transfer contributions. In this paper, we used  $\mu$  and  $J(\xi)$  to get insights into the specific interactions that drives the reaction.

The paper is organized as follows: Section 2 is devoted to introducing the theoretical descriptors used in characterizing the reactions. Section 3 deals with the computational details, and

in section 4, the results are presented and discussed. Section 5 contains some concluding remarks.

## 2. Theoretical Aspects

**2.1. Energy and Force Profile.** For any given elementary step of a chemical process, reactants must suffer a series of continuum structural changes to transform into products. The three-dimensional motion of atoms can be condensed to one intrinsic reaction coordinate (IRC)<sup>23–25</sup> in which energy is monitored for different structural configurations, generating a minimum energy path,  $E(\xi)$ , connecting the transition state to reactants and products. The derivative of  $E(\xi)$  with respect to the reaction coordinate  $\xi$ , is defined as the reaction force,<sup>26–28</sup> a global property of the system:

$$F(\xi) = -\frac{dE}{d\xi} \quad (2)$$

The critical points of the reaction force profile are the key points that divides the reaction path in reaction regions, in which different mechanism might be operating in order to keep the reaction going on. These points are a minimum at  $\xi_1$  and a maximum at  $\xi_2$ , thus defining the reactant region within the interval  $\xi_R \leq \xi \leq \xi_1$ , the transition state region at  $\xi_1 \leq \xi \leq \xi_2$  in which the transition state is located at  $\xi_0$  such that  $F(\xi_0) = 0$ . The product region is defined between  $\xi_2 \leq \xi \leq \xi_P$ . This feature set the basis to characterize any property along the IRC within the reaction regions,<sup>27–30</sup> and gives insights about specific effects that drives the reaction. In particular, the energy involved in these stages might be quantified through the amount of work done on the system within the different regions<sup>31–34</sup>

$$W_1 = -\int_{\xi_R}^{\xi_1} F(\xi) d\xi \quad (3)$$

$$W_2 = -\int_{\xi_1}^{\xi_2} F(\xi) d\xi \quad (4)$$

such that the energy barrier is  $\Delta E^\ddagger = W_1 + W_2$ . The nature of  $W_1$  is mainly associated with preparative structural changes,<sup>28,34</sup> whereas  $W_2$  has been attributed to electronic effects, since at the transition state region,<sup>28,31</sup> electronic properties dramatically changes thus indicating that the electron density is being redistributed along the new atomic connectivity, envisioning

\* To whom correspondence should be addressed.

product formation.<sup>28,33</sup> Although these conclusions might differ between chemical reactions, they enlightens us to search for structural and electronic parameters that can point out how and where electron transfer is taking place and which are the main factors that contribute to the reaction activation barrier, that is to say, to the reaction mechanism.

**2.2. Chemical Potential and Reaction Electronic Flux (REF).** From DFT variational minimization of the energy functional, the associated Lagrange multiplier is identified with the chemical potential  $\mu = (\partial E / \partial N)_{v(r)}$ , first order response of the energy to changes in the number of particles.<sup>19,20</sup> Despite we are not dealing with open systems, the measure of the escaping tendency of the whole electronic cloud is of great value for understanding the electron transfer processes during a chemical reaction. Numerical values of chemical potential are obtained using the finite difference approximation followed by the Koopmans Theorem,<sup>35</sup> thus giving approximate expressions for  $\mu$ <sup>17–20</sup>

$$\mu \approx -\frac{1}{2}(I + A) \approx \frac{1}{2}(\varepsilon_H + \varepsilon_L) \quad (5)$$

where  $I$  is the first ionization potential,  $A$  is the electron affinity, and  $\varepsilon_H$  and  $\varepsilon_L$  are the energies of the highest occupied and lowest unoccupied molecular orbitals, HOMO and LUMO, respectively.

The continuous variation of the chemical potential is followed along the reaction pathway, through infinitesimal changes for the series of non stationary points that comprises the IRC. The reaction electronic flux is then defined as the negative of the chemical potential gradient, with transport coefficient  $Q$ <sup>22</sup>

$$J(\xi) = -Q \left( \frac{d\mu}{d\xi} \right) \quad (6)$$

The development of this formulation is presented in previous studies of the energy dependence to changes in  $\mu$  and  $\eta$ ,  $E\{\mu, \eta\}$ ,<sup>26,36</sup> where an analytic expression for the transport coefficient  $Q$  is made available for specific cases in which the energy and the chemical potential present an important degree of correlation.<sup>26</sup> The characterization of electronic transport coefficients within the frame of the reaction electronic flux is an open issue that will be addressed elsewhere. In this paper  $Q = 1$  will be used to focus the analysis on the derivative of the chemical potential only.

Making the analogy with the free energy in macroscopic thermodynamic, eq 6 indicates that a positive reaction electronic flux will entail spontaneous changes in the electronic density, whereas negative  $J(\xi)$  values are related with non spontaneous electronic reordering. Going deeper into the macroscopic thermodynamics analogy, we can expect that during bond formation between reactants of different chemical potential  $\mu_A > \mu_B$ , there will occur an electron density transfer from A to B in order to stabilize the system and to fulfill  $\mu_A = \mu_B$  at equilibrium. This transfer can be analyzed through the decomposition of the total reaction electronic flux  $J(\xi)$ , into intra and intermolecular electronic contributions, characterized in terms of polarization effects  $J_p$  on each reactant and net charge transfer processes  $J_t$  between them

$$J(\xi) = J_p(\xi) + J_t(\xi) \quad (7)$$

where

$$J_p(\xi) = J_A(\xi) + J_B(\xi) \quad (8)$$

The polarization flux  $J_p(\xi)$  split into two contributions associated to the specific fragments involved in the reaction, as indicated by eq 8, will be determined through the use of the counterpoise<sup>37–39</sup>

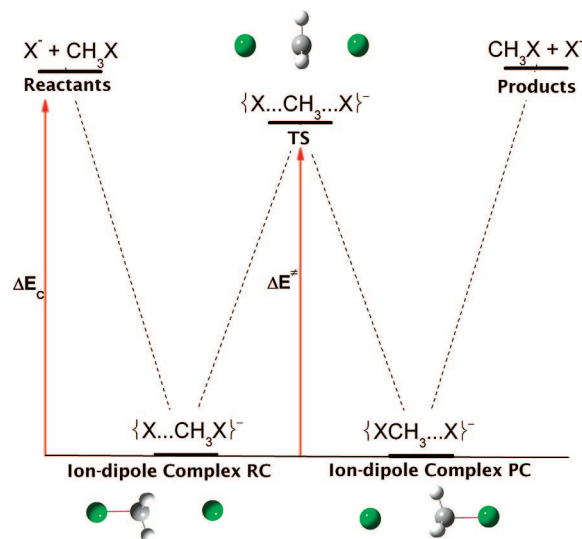


Figure 1. Energetic sketch for a generic  $S_N2$  reaction:  $XCH_3 + X^-$ .

method, designed for characterizing the basis set superposition error in molecular interactions within the supermolecule approach. Assuming that the fragmentation of the supermolecule holds all along the reaction coordinate, it is possible to obtain the chemical potential for the reaction participants at each point along the reaction coordinate. This provides a way to estimate the polarization fluxes  $J_A(\xi)$  and  $J_B(\xi)$  induced in fragments A and B by the presence of fragments B and A, respectively. In this way, the REF decomposition emerges as a powerful tool to discover charge transfer and polarization effects that are involved in the mechanism of chemical reactions.

### 3. Computational Details

All calculations were performed at the B3LYP/6-311++g\*\*<sup>40–43</sup> theory level, using the standard Gaussian 03<sup>44</sup> package. The characteristic  $S_N2$  collinear attack was ensured fixing the  $X-C-X$  angle at  $180^\circ$  during the transition state optimization, and the reaction path was followed by an IRC<sup>24,25</sup> type calculation in mass weighted internal coordinates<sup>45</sup> ( $\xi$  is given in  $\text{amu}^{1/2} \text{ bohr}$ ), between the two ion-dipole complexes, RC and PC (Figure 1).

For the specific cases studied here, the efficiency of the B3LYP hybrid functional to provide reliable reaction barriers was tested by making calculations using the functionals PBEPBE<sup>46</sup> and MPWPBE,<sup>46,47</sup> the results obtained using the standard 6-311++g\*\* basis set were also compared with the reference CCSD(T) calculations by Schaefer et al.<sup>14</sup> For **R1** the B3LYP barrier (8.42 kcal/mol) compares quite well with the coupled cluster calculation (8.13 kcal/mol), whereas the PBEPBE and MPWPBE calculations clearly underestimate the barrier (6.52 and 6.35 kcal/mol, respectively). Although in **R2** the three density functionals underestimate the CCSD(T) energy barrier (13.11 kcal/mol), the B3LYP functional (9.54 kcal/mol) still provides the best comparison; PBEPBE (6.55 kcal/mol) and MPWPBE (6.48 kcal/mol) values differ by a factor of 2 with respect to the reference CCSD(T) result.

Single-points calculations were performed at the already optimized IRC geometries in order to obtain energetic and electronic data, as well as  $\varepsilon_H$  and  $\varepsilon_L$  values to calculate the chemical potential  $\mu$  as indicated by the Koopmans theorem. It has been shown that, although the Koopmans theorem is defined

**TABLE 1: Energetic Parameters in kcal/mol for R1,  $\text{ClCH}_3 + \text{Cl}^-$ , and R2,  $\text{FCH}_3 + \text{F}^-$** 

	$\Delta E_C$	$\Delta E^\ddagger$	$W_1$	$\%W_1/\Delta E^\ddagger$	$\Delta\mu^\ddagger$
<b>R1</b>	−9.93	8.43	4.59	55%	−16.44
<b>R2</b>	−14.52	9.55	5.22	55%	−17.59

within the frame of the Hartree–Fock methodology, it can be applied to DFT calculations.<sup>48–50</sup> Studies on a variety of systems show that chemical potentials determined using the energy of the frontier molecular orbitals or the ionization potentials and electron affinities, present similar trends<sup>48,51,52</sup> so that it is expected that the derivative should not be affected by the use of either way of eq 5.

The counterpoise<sup>37</sup> routine was employed to calculate the polarization contribution to the REF from each of the reaction participants  $A = \text{XICH}_3$  and  $B = \text{X2}^-$ , as indicated by eq 8.

#### 4. Results and Discussion

**4.1. Energy and Reaction Force Profiles.** The first energetic parameter analyzed is the binding energy  $\Delta E_C$  of the ion-dipole complexes RC (Figure 1), as a measure of the X–C bond strength regarding the separated reactants. A stronger interaction for the fluorine (Table 1) is reported, about 4.5 kcal/mol above the chlorine complexation energy. This result can be attributed to the higher electronegativity and smaller size of the fluorine atom, allowing an stronger electrostatic interaction with the molecular fragment.<sup>53,54</sup> From RC, the reaction follows a symmetrical path leading to the product ion–dipole complex PC, surmounting the reaction activation barrier  $\Delta E^\ddagger$  (Table 1). The selectivity toward the halogen atom is lost, differing by about 1.1 kcal/mol between the chlorine reaction **R1** and the fluorine reaction **R2** (eq 1). As both reactions are symmetric (simultaneous bond breaking and formation), the thermodynamic factors related to the energy of broken and formed bonds are canceled for each process; therefore, the reaction activation barrier does not reflect the particular affinity of the carbon center for any of the two halogen atoms. Some other important contributions to the barrier height are the structural stress of the central carbon fragment<sup>55</sup> and the steric repulsion between it and the entering nucleophile,<sup>56</sup> which are equivalent for **R1** and **R2** since the same methyl center is considered.

Energy and reaction force profiles are comparatively presented in Figure 2 for **R1** and **R2**. The critical points  $\xi_1$  and  $\xi_2$  (dashed vertical lines in the reaction force profiles), define the reaction regions that will frame our study, allowing the energetic barrier decomposition in terms of the work invested in each region, in order to reach the highly delocalized transition structure. Values of  $W_1$  are reported in Table 1, showing that the energetic weight of  $W_1$  upon the activation barrier is the same for both reactions, a 55% of each  $\Delta E^\ddagger$ . Despite the differences in the RC initial bond strength, **R1** and **R2** have the same energetic degree of advance at  $\xi_1$ . An initial slope analysis of the reaction force profile, shows the evolution of the forces opposing the preparation step in the reactants region, denoting a change in the nature of the  $\text{C}\cdots\text{X2}$  bond.

As described in the introduction, the  $\text{S}_{\text{N}}2$  structural mechanism is a collinear attack, in which the main feature is the carbon-halogen interatomic distance. Figure 3 displays the evolution of the  $\text{X1}-\text{CH}_3$  and  $\text{X1CH}_3\cdots\text{X2}$  distances along the reaction coordinate  $\xi$  for both processes. The most noticeable feature is that as the nucleophile approaches to the methyl center, after a preparative stage where the  $\text{X1}-\text{CH}_3$  bond distance does not change, the leaving group goes away reaching the same rate of the incoming atom. The preparative stage last until a

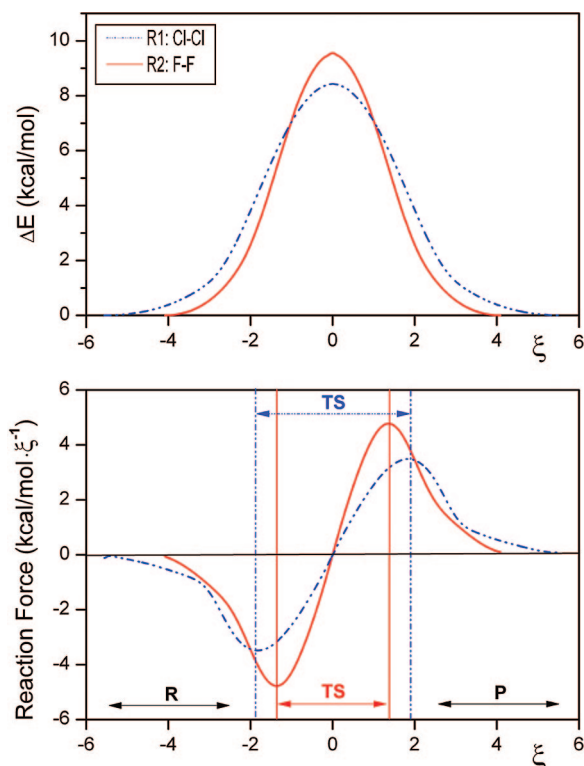


**Figure 2.** Energy and force profiles for **R1**,  $\text{ClCH}_3 + \text{Cl}^-$ , and **R2**,  $\text{FCH}_3 + \text{F}^-$ . The reaction coordinate  $\xi$  is given in  $\text{amu}^{1/2}\text{bohr}$ .

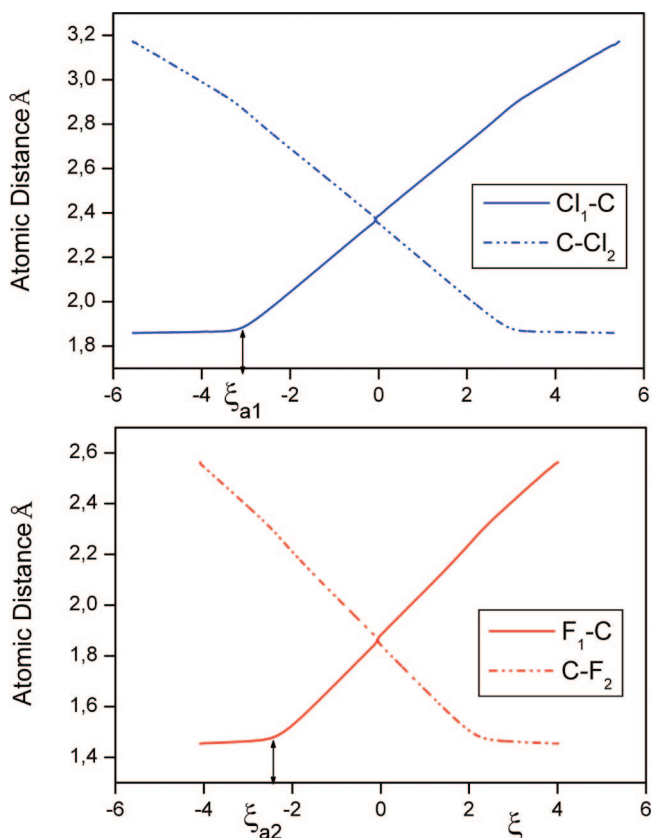


**Figure 3.** Halide-carbon atomic distance profiles **R1** and **R2**.

certain nucleophile proximity, 1.88 Å at  $\xi \approx -3.2$  for **R1** and 1.48 Å at  $\xi \approx -2.5$  for **R2** (shown by arrows in Figure 3).

In a first approximation to the electronic structure study, dipole moment (DM) profiles along the IRC provide a balanced vision of both structural and electronic reorders, reflecting the



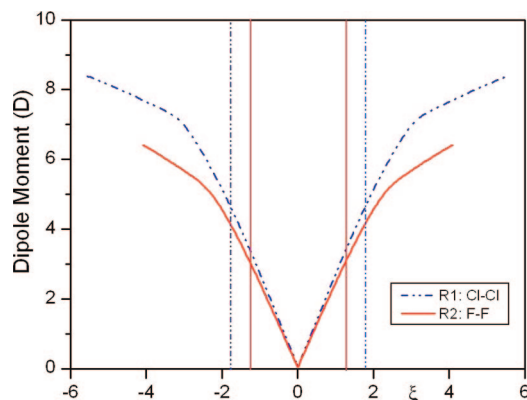


Figure 4. Dipole moment profiles for **R1** and **R2**.

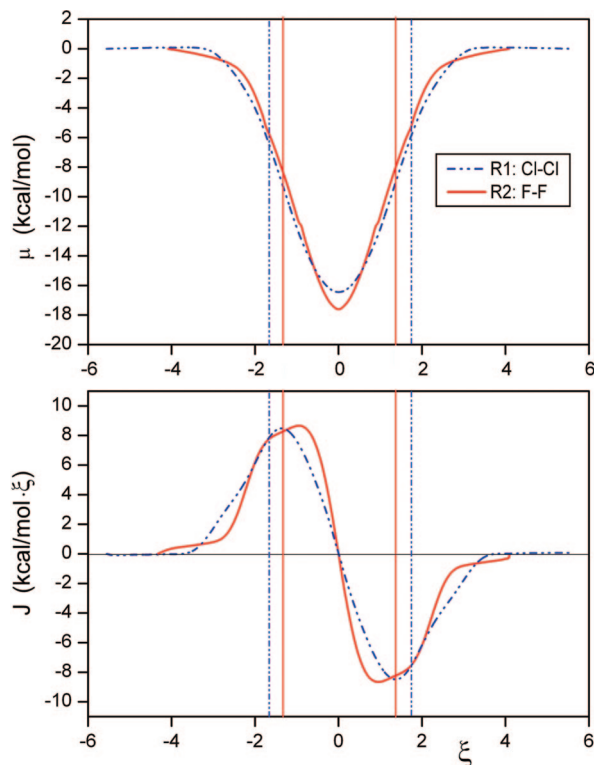


Figure 5. Chemical potential and electronic flux profiles for **R1** and **R2**.

evolution of the molecular charge distribution (Figure 4). Three main features stand out: a higher DM initial value for **R1**, about 2 D above **R2**, in accordance with a less strong binding energy  $\Delta E_C$ ; a slope discontinuity in the reactant region at the same reaction coordinate observed in the reaction force and bond distance profiles ( $\xi_{a1} = \pm 3.2$  and  $\xi_{a2} = \pm 2.5$ ); and a fast charge equalization in the transition state region in order to reach  $DM_{(TS)} = 0$ , due to the symmetrical distribution of the electron density along the  $X1-C-X2$  axis. From now on, in order to simplify further analysis, the reaction coordinate corresponding to the activation inflection points will be referred as  $\xi_{a1}$  for **R1** and  $\xi_{a2}$  for **R2**.

#### 4.2. Chemical Potential and Reaction Electronic Flux.

**4.2.1. General Features of the  $\mu(\xi)$  and  $J(\xi)$  Profiles.** Moving forward on the electronic structure analysis, Figure 5 shows, in a comparative way, the chemical potential profile for **R1** and **R2**, relative to reactants. The changes between RC and the transition state ( $\Delta\mu^\ddagger$ ) are very significant, about  $-17$  kcal/mol each (Table 1). This implies that the TS configuration has lower electron escaping tendency, a measure of the stability of

the highly delocalized electronic cloud. There is no significant difference between the  $\Delta\mu^\ddagger$  barriers for **R1** and **R2**, characterizing general features of the methyl halide substitution. Relative to the initial slopes of the curves, once again there is evidence of an activation process in the reactant region, that after  $\xi_{a1}$  and  $\xi_{a2}$ , breaks out a rapid electron cloud redistribution in the TS region, just as in the DM profile.

In order to explore in depth the electron redistribution caused by the chemical potential equalization, the REF profile  $J(\xi)$  is analyzed (Figure 5), producing interesting results. **R1** has no flux during the first part of the reactant region (from RC to  $\xi_{a1}$ ), providing evidence for a strictly electrostatic interaction between the halogen atom and the methyl-halide fragment. In contrast, **R2** presents a small basal electronic flux (from RC to  $\xi_{a2}$ ), which is consistent with a higher complexation energy  $\Delta E_C$ , due to a stronger  $X2\cdots C$  bond in the reactive complex. In a second instance, once each nucleophile reaches  $\xi_{a1}$  and  $\xi_{a2}$ , both reactions are activated by an important reaction electronic flux, which allows to overcome the preparative stage in order to initiate the simultaneous bond breaking and formation process. **R1** reaches a single maximum in the TS region, whereas **R2** features an incipient shoulder before  $\xi_1$  and a maximum after  $\xi_1$ , as a first evidence of different charge distribution mechanisms, attributable to different initial bond strength and/or nature.

It has been established that the reaction coordinate segmentation given by the force profile clearly frames the activation phenomena in the reactant region, showing that its energetic cost is proportionally equivalent for **R1** and **R2** (a 55% of each barrier). If we consider the different initial binding energies  $\Delta E_C$ , it is reasonable to expect dissimilar charge transfer mechanism, in order to minimize the energetic expense of the monovalent anion exchange. The REF decomposition, together with an NBO analysis will enlighten this fact.

Aside, it is important to point out that the TS geometry gathers some special features, becoming a balance point: despite being thermodynamically unstable, the electronic properties are equilibrated with the reaction driving forces, characterized by  $F(\xi_0) = 0$ ,  $DM(\xi_0) = 0$  and  $J(\xi_0) = 0$ .

**4.2.2. REF Decomposition.** The REF decomposition shows different charge distribution mechanism for the two studied reactions. In Figure 6 the results are presented comparatively in terms of polarization effects  $J_p(\xi)$  on each reactant and net charge transfer processes between them  $J_t(\xi)$ , along with the total flux  $J(\xi)$ . Due to the reaction symmetry and for the sake of an enhanced information display, the profiles are presented from the reaction complex RC to the transition state coordinate only.

For the chlorine substitution **R1**, it is found that the zero flux region observed in the  $J(\xi)$  profile is not the consequence of a cancelation between  $J_p(\xi)$  and  $J_t(\xi)$ , but a genuine electrostatic interaction region. As the nucleophile approaches, once a certain  $Cl1CH_3\cdots Cl2$  distance of 2.8 Å is reached, a rapid polarization flux  $J_p(\xi)$  emerges, presenting its maximum at  $\xi = -2.3$ , a few steps after  $\xi_{a1}$ , then  $J_p(\xi)$  is sustained along the transition state region, generating intramolecular charge redistribution until the TS configuration. The polarization flux activates an initially non spontaneous transfer flux  $J_t(\xi) < 0$ , that increases constantly in order to reach its maximum around  $\xi = -1.29$ , corresponding to the maximum of  $J(\xi)$ . The maximum REF observed at the transition state region is due, in almost the same extent, to polarization and transfer effects. At the TS configuration the zero flux is attained by cancelation of the two contributions  $J_p(\xi)$  and  $J_t(\xi)$ .

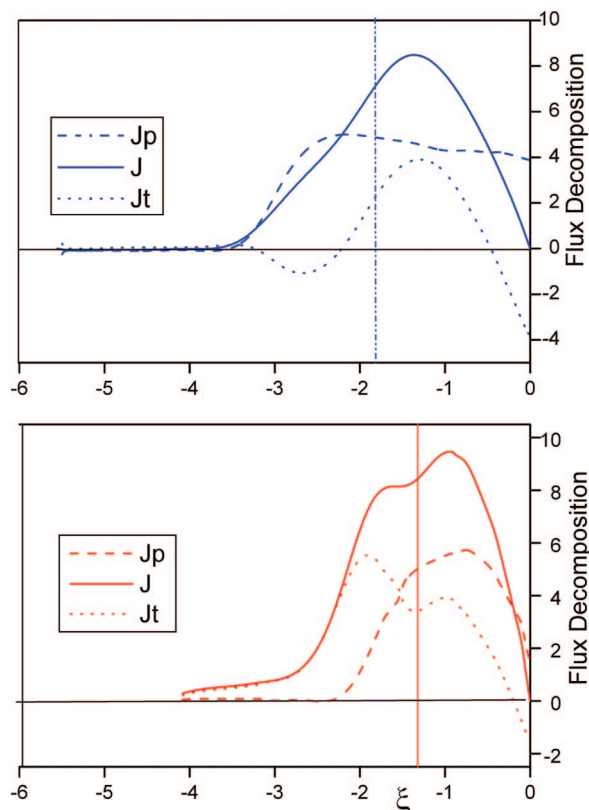


**Figure 6.** Electronic flux decomposition profiles for **R1** and **R2**. The electronic flux is given in kcal/mol·ξ.

A different behavior of the REF is observed for the fluorine substitution **R2**. The small positive (spontaneous) reaction electron flux present since the reactive complex formation corresponds to pure transference flux, generating a much more strong bond for the reactive complex RC, than the corresponding purely electrostatic one. The nucleophile approach enhances this interaction, rising the transference flux considerably after  $\xi_{a2}$ , reaching a first maximum as it approaches to  $\xi_1$ . The REF incipient shoulder is therefore mostly due to electron transfer effects. At the same time,  $J_t(\xi)$  activates a polarization response  $J_p(\xi)$  which is completed in the transition state region. This internal charge redistribution phenomena is accompanied by a new local maximum in  $J_t(\xi)$ , corresponding to the second hump in the  $J(\xi)$  profile which in turn is now mostly due to polarization effects. Both components of the REF tend to decrease toward the TS geometry, showing that the major electronic rearrangements were completed in the first part of the TS region.

**4.2.3. Natural Population Analysis.** Figure 7 displays the natural charge profiles for the three main atomic centers on each reaction, adding some valuable information in order to support the electronic flux decomposition. Consistently with our previous observations, the charge profiles exhibit activation inflection points at  $\xi_{a1}$  and  $\xi_{a2}$ . In the **R1** profile, initial atomic charge values remain constant until  $\xi_{a1}$ , confirming purely electrostatic interactions in the first half of the reactants region. Afterward, the REF break out symmetric charge equalization between the entering and leaving halide, passing by a crossing point in the TS: maximum charge delocalization is reached in the equally distanced bonds, framing the major electronic reorders into the TS region.

By observing the ratio of the halogens to the carbon center charge, it is possible to conclude some features about the reaction bond nature. Initially, the carbon charge is framed

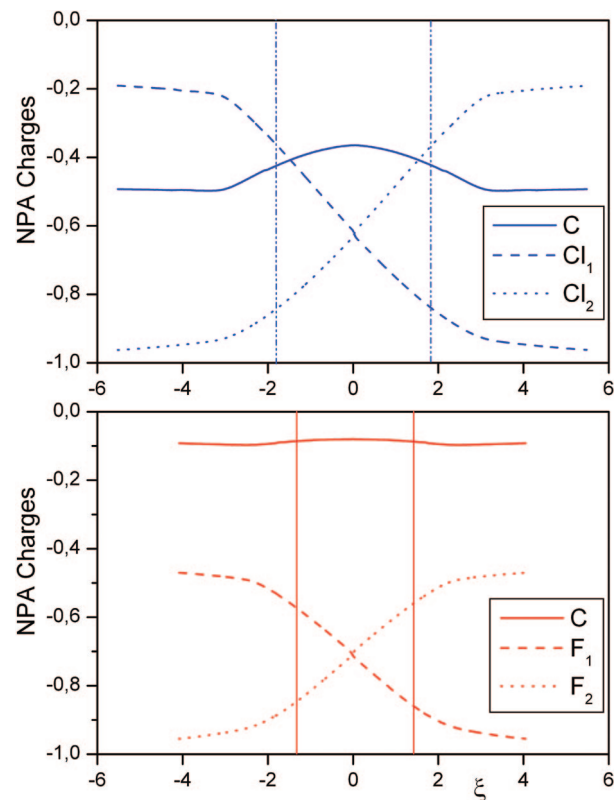


**Figure 7.** NPA charge profiles for **R1** and **R2**.

**TABLE 2: NPA and NBO Parameters for R1, Atomic Charges and Bond Populations**

	C	Cl1	Cl2	$\sigma_1$	$\sigma_1^*$	$n_{Cl2}$	$\sigma_2$	$\sigma_2^*$
RC	-0.492	-0.190	-0.963	1.996	0.038	1.964		
$\xi_{a1}$	-0.496	-0.217	-0.934	1.996	0.064	1.935		
$\xi_1$	-0.423	-0.366	-0.840	1.995	0.156	1.841		
TS	-0.365	-0.613	-0.633	1.996	0.351	1.634		

**TABLE 3: NPA and NBO Parameters for R2, Atomic Charges and Bond Populations**

	C	F1	F2	$\sigma_1$	$\sigma_1^*$	$n_{F2}$	$\sigma_2$	$\sigma_2^*$
RC	-0.092	-0.470	-0.955	1.997	0.041	1.960		
$\xi_{a2}$	-0.097	-0.492	-0.923	1.996	0.067	1.928		
$\xi_1$	-0.085	-0.580	-0.839	1.994	0.147	1.841		
TS	-0.079	-0.702	-0.713	1.887	0.182		1.884	0.179

between the chlorines charge, revealing covalent bond interaction. The carbon-halide bond in the chloromethane moiety is characterized by an extensive density overlap, with a high negative charge on the carbon  $-0.492$  and a low charge value of  $-0.190$  on the chlorine (Table 2). Once the transition state is reached, the ratio changes because the carbon charge has been decreased up to  $-0.365$ , while both halogens charge lie under this value, suggesting that certain ionic character emerges. At the same time, the charge evolution of the carbon center along the reaction coordinate enlightens the substitution interactions, showing sensibility to the nucleophile exchange. As the electron transfer is activated, the NPA charges are affected, reflecting the predominance of through bond interactions<sup>57</sup> within the charge transfer mechanism.

In terms of the REF, the sudden polarization of the methyl halide fragment ( $J_p(\xi)$  rise), activates the initially non spontaneous ( $J_t(\xi) < 0$ ) transference flux between the substitution participants, responsible for the partial (and

symmetric) bond breaking and formation process. These reorderings are reflected in the gradual carbon center charge loss, acting as a bridge between the two partially bonded chlorine atoms. After the  $J_t(\xi)$  max, the polarization flux is responsible for the electron density redistribution, in order to attain a highly delocalized transition structure.

The **R2** NPA profile shares general features with the **R1** profile: the entering and leaving halide present a characteristic  $S_N2$  symmetric charge evolution with respect to the transition state, activated in the reactants region ( $\xi_{a2}$ ) and mainly located in the TS region. However, a distinctive feature of reaction **R2** is found on the carbon charge and its evolution. Initially it is not framed between the fluorines charges, but above them with a small value of  $-0.092$  (practically neutral), reflecting the ionic character of the methyl-halide bond. This charge value will remain practically constant during the substitution process (Table 3), as a sign of through space<sup>57</sup> interactions in order to achieve the charge equalization. As the entering halogen approaches, a partial bond starts to develop with the molecular fragment, generating the first  $J_t(\xi)$  maximum. Note that the fluorine is a small atom, so the transfer phenomena precedes the polarization one: at the first  $J_t(\xi)$  max  $J_p(\xi)$  start to rise, completing the density delocalization along the X–C–X axis. In the simultaneous bond breaking and formation, through space interactions must predominate, otherwise, the charge on the carbon center will reflect a partial accumulation or depletion, as it did in the **R1** profile.

**4.2.4. Natural Bond Orbital Analysis.** It results very interesting to contrast the REF study with the classical chemical picture provided by the NBO bond analysis.<sup>58</sup> The electronic structure of the studied compounds is rationalized in terms of a Lewis type bond net, where localizing bonds ( $\sigma$ ) and lone pairs ( $n$ ) are basic units for molecular assembly. Antibonding orbitals ( $\sigma^*$ ) are used to describe non covalent effects and Rydberg orbitals ( $ry$ ) for delocalization effects, representing unused valence shell capacity. As for the NPA, the bond evolution was followed all along the reaction pathway. Tables 2 and 3 displays the main results for the critical points of the reaction profile: reactants (RC),  $\xi_a$ ,  $\xi_1$ , and TS geometry.

The RC configuration of **R1**, presents a proper covalent bond  $\sigma_1$  (Figure 8), and its corresponding antibond  $\sigma_1^*$ , with an occupation number of 0.038, provided trough an interaction with the entering chlorine  $Cl2$  lone pair, a 3p orbital with its population decreased to 1.964. As the reaction moves forward on the reactant region, the outbreak of the reaction electronic flux occurs in  $\xi_{a1}$  which is characterized by the first interaction from the molecular fragment  $\sigma_1$  to a delocalized Rydberg orbital of the  $Cl2$  nucleophile. Despite being a really small interaction (0.004 transferred), it marks the beginning of a deeper rapport of the electronic clouds, with a retrodonation phenomena that will remain until the TS configuration.

After  $\xi_{a1}$ ,  $J_p$  reaches its maximum value at  $\xi \approx -2.7$ , coinciding with the appearance of charge transfer from  $\sigma_1$  and  $\sigma_1^*$  orbitals to delocalized  $ry^*$  orbitals on the chlorine and carbon atoms that form the corresponding bond. The charge density is redistributed in the chloromethane moiety in order to prepare the leaving group, reflecting the connection between the reaction polarization flux  $J_p$  and internal charge transfer processes, confirming through bond polarization in order to delocalize the transferred charge. On the other hand, the charge transfer from the lone pair to the antibonding  $\sigma_1^*$  increases continuously, while the  $\sigma_1$  population remains constant at 1.995, showing that the  $\sigma_1^*$  is populated completely from the entering lone pair.

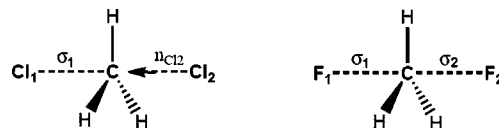


Figure 8. Transition state bond sketches, **R1** and **R2**.

Finally, in the transition state configuration no proper C–Cl<sub>2</sub> bond is generated ( $\sigma_2$ ), explaining the steady polarization phenomena observed in Figure 6, in order to delocalize the charge coming from the  $n_{Cl2} \rightarrow \sigma_1^*$  transfer. Noncovalent effects are enhanced, reflecting a growing ionic character in the bond evolution, in agreement with our previous observations on the **R1** charge profile. This behavior might be attributed to a high electronegativity and chlorine size, capable of retaining much more electron density than the compared fluorine anion.

The fluorine substitution presents the same initial bond net than the chlorine one. The ion-dipole complex is formed by an  $n_{F2} \rightarrow \sigma_1^*$  interaction, toward the fluoromethane moiety, with an small charge transfer of 0.041. As the reaction moves forward, once again the activation point  $\xi_{a2}$  coincides with the establishment of retrodonations from the molecular fragment to the entering fluorine F2, a  $\sigma_{CH} \rightarrow ry_{F2}^*$  interaction, involving this time the three C–H bonds instead of only the  $\sigma_1$  bond in **R1**, illustrating the through space interaction pattern.

The distinctive **R2** reaction feature occurs at the  $J_t(\xi)$  second maximum, which exactly coincides with the formation of a new bond between the entering fluorine and the molecular fragment, generating a pentacoordinate carbon center. Before reaching the transition state and after  $\xi_1$ , the preexistent  $\sigma_1$  bond has a small population decrease to 1.918, while the  $n_{F2}$  transfers its population to the new  $\sigma_2$  bond to reach 1.861. From this point on, the main feature will be an electron delocalization processes through  $\sigma_1 \rightarrow \sigma_2^*$  crossed charge transfer to attain the equally populated  $\sigma_1$  and  $\sigma_2$  bonds, enhancing the ionic character of the transition state configuration.

Aside, if we compare the **R1** and **R2**  $n_{X2}$  populations at  $\xi_1$ , the same value is encountered 1.841 (Tables 2 and 3), along with a revealing feature: at this point the  $\sigma_1 \rightarrow \sigma_1^*$  interactions are established for the first time in both reactions. If we recall that the energetic degree of advance was equivalent at the same point (55% of  $\Delta E^\ddagger$ ), we can attribute this energy investment to the population decrease of the entering lone pair  $n_{X2}$  from 1.996 to 1.841 in both reactions. The structural rearrangements observed in Figure 3 appear clearly related to the electronic transfer and its energetic cost: despite having a different charge transfer mechanism, common features relates both processes, implying that reaction peculiarity is mostly developed in the transition state region.

## 5. Concluding Remarks

The concerted  $S_N2$  mechanism is recovered for the chlorine and fluorine identity reactions. Bond distances and atomic charges evolve symmetrically, generating an equivalent energetic pattern that goes from ion–dipole complexes to a highly delocalized transition structure, characterized by a minimum electron escaping tendency ( $\Delta\mu_{min}^\ddagger$ , DM = 0). In this context, the reaction coordinate segmentation, provided by the reaction force analysis, shows to be an unambiguous and natural way to elucidate the reaction mechanism.

For both processes, the reaction activation occurs in the reactants region and it is related with structural parameters (entering nucleophile proximity), along with a peculiar electronic density response in each case: the reaction electronic flux and



its decomposition revealed different charge transfer mechanism for the studied reactions. The chlorine substitution is activated by a polarization flux, while the fluorine substitution is activated by a transference flux. These features are clearly exposed in the transition state region, where the major electronic reorders take place.

Polarization effects drive the **R1** substitution, with a continuous charge redistribution along the chloromethane moiety in order to allow the nucleophile exchange, dominated by through bond interactions. On the contrary, the **R2** substitution is driven by transference flux, redistributing electron density by means of through space interactions, leading to the formation of a new bond, in agreement with the fluorine smaller size. The REF decomposition analysis, together with the reaction force analysis prove to be a powerful tool to elucidate reaction mechanism, with a high sensibility to electron density changes.

**Acknowledgment.** The authors thank FONDECYT for financial support through project No. 1060590 and FONDAP through project No. 11980002 (CIMAT). E.E. is grateful to CONICYT for a graduate fellowship.

## References and Notes

- Hase, W. *Science* **1994**, 266, 998–1002.
- Bohme, D. K.; Young, L. B. *J. Am. Chem. Soc.* **1970**, 92, 7354.
- Bohme, D. K.; Mackay, G. I.; Payzant, J. D. *J. Am. Chem. Soc.* **1974**, 96, 4027.
- Olmstead, W.; Brauman, J. *J. Am. Chem. Soc.* **1977**, 99, 4219.
- Rossi, R. A.; Pierini, A. B.; Peññory, A. B. *Chem. Rev.* **2003**, 103, 71.
- Ritchie, C. D.; Chappell, G. A. *J. Am. Chem. Soc.* **1970**, 92, 1819.
- Dedieu, A.; Veillard, A. *J. Am. Chem. Soc.* **1972**, 94, 6730.
- Dedieu, A.; Veillard, A. *J. Am. Chem. Soc.* **1973**, 95, 7715.
- Morokuma, K. *J. Am. Chem. Soc.* **1982**, 104, 3732.
- Vande Linde, S. R.; Hase, W. L. *J. Phys. Chem.* **1990**, 94, 2778.
- Hô, M.; Schmider, H. L.; Weaver, D. F.; Smith, V. H.; Sagar, R. P.; Esquivel, R. *Int. J. Quantum Chem.* **1999**, 77, 376–382.
- Parthiban, S.; Oliveira, G.; Martin, J. M. L. *J. Phys. Chem.* **2001**, 105, 895–904.
- Gonzales, J.; Pack, C.; Cox, R. S.; Allen, W.; Schaefer, H. F. *Chem.-Eur. J.* **2003**, 9, 2173.
- Gonzales, J.; Allen, W.; Schaefer, H. F. *J. Phys. Chem. A* **2005**, 109, 10613–10628.
- Chattaraj, P. K.; Roy, D. R. *J. Phys. Chem. A* **2006**, 110, 11401.
- Joubert, L.; Pavone, M.; Barone, V.; Adamo, C. *J. Chem. Theory Comput.* **2006**, 2, 1220–1227.
- Parr, R. G.; Yang, W. *Density Functional Theory of Atoms and Molecules*; Oxford University Press: New York, 1997.
- Geerlings, P.; Proft, F. D.; Langenaeker, W. *Chem. Rev.* **2003**, 103, 1793–1873.
- Parr, R. G.; Donnelly, R.; Levy, M.; Palke, W. *J. Chem. Phys.* **1978**, 68, 3801.
- Sen, K. D.; Joergensen, C., Eds.; *Structure and Bonding: Electronegativity*; Springer-Verlag: Berlin, 1987; Vol. 66.
- Padmanabhan, J.; Parthasarathi, R.; Subramanian, V.; Chattaraj, P. K. *J. Phys. Chem. A* **2007**, 111, 1358.
- Herrera, B.; Toro-Labbé, A. *J. Phys. Chem. A* **2007**, 111, 5921.
- Fukui, K. *J. Phys. Chem.* **1970**, 74, 4161.
- Fukui, K. *Acc. Chem. Res.* **1981**, 14, 363.
- Gonzalez, C.; Schlegel, H. B. *J. Phys. Chem.* **1989**, 90, 2154.
- Toro-Labbé, A. *J. Phys. Chem. A* **1999**, 103, 4398.
- Herrera, B.; Toro-Labbé, A. *J. Phys. Chem.* **2004**, 121, 7096.
- Gutiérrez-Oliva, S.; Herrera, B.; Toro-Labbé, A.; Chermette, H. *J. Phys. Chem. A* **2005**, 109, 1748.
- Burda, J. V.; Toro-Labbé, A.; Gutiérrez-Oliva, S.; Murray, J. S.; Politzer, P. *J. Phys. Chem. A* **2007**, 111, 2455.
- Rincón, E.; Jaque, P.; Toro-Labbé, A. *J. Phys. Chem. A* **2006**, 110, 9478.
- Politzer, P.; Toro-Labbé, A.; Gutiérrez-Oliva, S.; Herrera, B.; Jaque, P.; Concha, M.; Murray, J. *J. Chem. Sci.* **2005**, 117, 467.
- Politzer, P.; Burda, J. V.; Concha, M. C.; Lane, P.; Murray, J. S. *J. Phys. Chem. A* **2006**, 110, 756–761.
- Rincón, E.; Toro-Labbé, A. *Chem. Phys. Lett.* **2007**, 438, 93.
- Toro-Labbé, A.; Gutiérrez-Oliva, S.; Murray, J.; Politzer, P. *Mol. Phys.* **2007**, 105, 2619.
- Koopmans, T. *Physica* **1993**, 91, 651.
- Cárdenas-Jirón, G.; Gutiérrez-Oliva, S.; Melin, J.; Toro-Labbé, A. *J. Phys. Chem. A* **1997**, 101, 4621.
- Boyd, S.; Bernardi, F. *Mol. Phys.* **1970**, 19, 553.
- Simon, S.; Duran, M.; Dannenberg, J. J. *J. Chem. Phys.* **1996**, 105, 11024.
- Salvador, P.; Fradera, X.; Duran, M. *J. Chem. Phys.* **2000**, 112, 10106.
- Becke, A. D. *J. Chem. Phys.* **1993**, 98, 5648–5652.
- Lee, C.; Yang, W.; Parr, R. G. *Phys. Rev. B* **1988**, 37, 785.
- Stephens, P. J.; Devlin, F. J.; Chabalowski, C. F.; Frisch, M. J. *J. Phys. Chem.* **1994**, 98, 11623.
- McLean, A. D.; Chandler, G. S. *J. Chem. Phys.* **1980**, 72, 5639.
- Frisch, M. J.; Trucks, G. W.; Schlegel, H. B.; Scuseria, G. E.; Robb, M. A.; Cheeseman, J. R.; Montgomery, J. A.; Vreven, T.; Kudin, K. N.; Burant, J. C.; Millam, J. M.; Iyengar, S. S.; Tomasi, J.; Barone, V.; Mennucci, B.; Cossi, M.; Scalmani, G.; Rega, N.; Petersson, G. A.; Nakatsuji, H.; Hada, M.; Ehara, M.; Toyota, K.; Fukuda, R.; Hasegawa, J.; Ishida, M.; Nakajima, T.; Honda, Y.; Kitao, O.; Nakai, H.; Klene, M.; Li, X.; Knox, J. E.; Hratchian, H. P.; Cross, J. B.; Bakken, V.; Adamo, C.; Jaramillo, J.; Gomperts, R.; Stratmann, R. E.; Yazyev, O.; Austin, A. J.; Cammi, R.; Pomelli, C.; Ochterski, J. W.; Ayala, P. Y.; Morokuma, K.; Voth, G. A.; Salvador, P.; Dannenberg, J. J.; Zakrzewski, V. G.; Dapprich, S.; Daniels, A. D.; Strain, M. C.; Farkas, O.; Malick, D. K.; Rabuck, A. D.; Raghavachari, K.; Foresman, J. B.; Ortiz, J. V.; Cui, Q.; Baboul, A. G.; Clifford, S.; Cioslowski, J.; Stefanov, B. B.; Liu, G.; Liashenko, A.; Piskorz, P.; Komaromi, I.; Martin, R. L.; Fox, D. J.; Keith, T.; Al-Laham, M. A.; Peng, C. Y.; Nanayakkara, A.; Challacombe, M.; Gill, P. M. W.; Johnson, B.; Chen, W.; Wong, M. W.; Gonzalez, C.; Pople, J. A. *Gaussian 03*, revision B.03; Gaussian, Inc.: Pittsburgh, PA, 2003.
- Gonzalez, C.; Schlegel, H. B. *J. Phys. Chem.* **1990**, 94, 5523.
- Perdew, J.; Burke, K.; Ernzerhof, M. *Phys. Rev. Lett.* **1996**, 77, 3865.
- Adamo, C.; Barone, V. *J. Chem. Phys.* **1998**, 10, 8–664.
- Cárdenas-Jirón, G.; Letelier, J.; Toro-Labbé, A. *J. Phys. Chem. A* **1998**, 102, 7864.
- Gutiérrez-Oliva, S.; Letelier, J.; Toro-Labbé, A. *Mol. Phys.* **1999**, 96, 61.
- Politzer, P.; Abu-Awwad, F. *Theor. Chem. Acc.* **1998**, 99, 83.
- Nath, S.; Sannigrahi, A.; Chattaraj, P. *J. Molec. Struct. (THEOCHEM)* **1994**, 306, 87.
- Toro-Labbé, A.; Zavallos, J. *J. Chil. Chem. Soc.* **2003**, 48, 717.
- Glukhovtsev, M.; Pross, A.; Radom, L. *J. Am. Chem. Soc.* **1995**, 117, 2024.
- Huheey, J. E.; Keiter, E. A.; Keiter, R. L. *Inorganic Chemistry, Principles of Structure and Reactivity*; Harper Collins College Publishers: London, 1981.
- Shaik, S. S.; Schlegel, H. B.; Wolfe, S. *Theoretical Aspects of Physical Organic Chemistry*; J. Wiley and Sons, Inc.: New York, 1992.
- Bento, A. P.; Bickelhaupt, F. M. *J. Org. Chem.* **2007**, 72, 2201–2207.
- Bulat, F.; Toro-Labbé, A. *Chem. Phys. Lett.* **2002**, 354, 508–517.
- Reed, A. E.; Curtiss, L. A.; Weinhold, F. *Chem. Rev.* **1988**, 88, 899.